Flexible Direction-of-Arrival Simulation for Automotive Radar Target Simulators

PIRMIN SCHOEDER (Graduate Student Member, IEEE), **VINZENZ JANOUDI**,
BENEDIKT MEINECKE (Graduate Student Member, IEEE),
DAVID WERBUNAT (Graduate Student Member, IEEE),
AND CHRISTIAN WALDSCHMIDT (Senior Member, IEEE)

(Regular Paper)

Institute of Microwave Engineering, Ulm University, 89077 Ulm, Germany

CORRESPONDING AUTHOR: Pirmin Schoeder (e-mail: pirmin.schoeder@uni-ulm.de).

ABSTRACT In order to simulate realistic traffic scenarios, a radar target simulator must be able to generate multiple radar targets with different directions of arrival. The presented concept is able to generate an arbitrary amount of targets with individual directions of arrival for the radar under test. By measuring the radar channel, the novel approach enables target simulators to simulate arbitrary directions of arrival, while minimizing the required hardware. The optimum setup is derived for radars with a uniform linear receive antenna array. The compensation of placement errors for automotive chirp-sequence frequency modulated continuous wave radars is demonstrated. Finally, the calibration for the setup is provided, and the performance of the presented approach is validated.

INDEX TERMS Automotive radar, chirp-sequence modulation, direction of arrival, FMCW radar, radar target simulator.

I. INTRODUCTION

The usage of radar sensors in automotive applications is rapidly increasing [1]. The robustness offered by radar detection makes the employment for advanced driver assistance systems (ADAS) highly attractive [2], [3]. With higher levels of autonomous functionality, thorough testing is required in order to ensure safe operation. To demonstrate the safe operation of an autonomous vehicle, hundreds of millions of test kilometers would be required [4]. By simulating various traffic scenarios with the help of a radar target simulator, the costs and time for test drives can be reduced significantly. In addition, specific traffic scenarios are completely reproducible and could therefore be used as a benchmark for comparing different radar systems or development iterations thereof. In a typical traffic scenario, like an intersection, many objects at different ranges, velocities, and directions are present at the same time. A radar target simulator suitable for the validation and testing of complex ADAS must be able to reproduce those

scenarios accurately. While there is a vast variety of concepts for the generation of radar targets with variable distances and velocities [5]–[8], there are only a few concepts for the generation of targets with a specific direction of arrival (DoA). The DoA of targets allows radar systems to estimate the position and orientation of other road users [9] or obstacles [10] and must be simulated as well for a realistic simulation. A test environment that is able to generate multiple targets with different DoAs for an automotive radar sensor was presented in [11] and [12]. The generation of the angular information relies on a mechanical approach that moves the target simulator antenna to the position of the intended DoA. This means the approach enables the target simulator to generate as many targets with an individual DoA at the same time, as there are movable antennas. Another approach was presented in [13], where low-cost modulated reflectors have a fixed position and therefore simulate a fixed DoA. For an entire automotive scenario that might have a field of view of $60°$, this approach

would require 30 target simulators for a resolution of $2°$. Similar approaches with two-dimensional antenna grids have been proposed in [14], [15].

In this article a novel approach for the generation of targets with flexible DoA is presented. By using coherently modulated target elements placed around the radar sensor under test, a joint DoA simulation is possible. Via electrical steering, the DoA of each individual target in the simulated scenario is generated, allowing the simulation of continously changing DoAs. Besides, the amount of different DoAs that can be simulated at the same time is not limited. Due to the electrical steering, no mechanically moving parts are employed, reducing costs and enhancing the overall reliability. Therefore, the simulation environment has a lower complexity, in comparison to mechanical solutions [11], [12]. Besides that, the restriction of a limited number of targets with individual DoA is resolved. The amount of required hardware is reduced significantly in comparison to a simulation environment that employs a target simulator for each simulated DoA [13]–[15]. The new concept is built on simple hardware and sophisticated signal processing, yielding a low-cost system.

The structure of this article is as follows. First, in Section II a general overview of the system is given. In Section III the mathematical description of the system and the simulation of targets with individual DoA is derived. The compensation of path length differences and the optimal positions for the radar and target simulator are analyzed. Afterwards, in Section IV the calibration process for the employment of the concept is presented. Simulation results of the influence of placement errros on the achievable DoA accuracy are presented in Section V. Lastly, measurements with a radar sensor and a target simulator, based on the proposed concept, are presented in Section VI, and the conclusion is given in Section VII.

II. SYSTEM CONCEPT

In the following a chirp-sequence frequency modulated continuous wave (CS-FMCW) radar sensor is assumed to be the radar under test. While the general concept for the DoA simulation is not restricted to CS-FMCW radars, this article focuses on radars employing the CS-FMCW modulation, since this is the state-of-the-art waveform in the automotive industry [1]. The system concept is based on N distributed target elements (TE) that are placed around the CS-FMCW radar sensor. The TEs are located at different azimuth angles but at the same distance in respect to the radar under test, as shown in Fig. 1. Each TE receives the transmit signal of the radar with an antenna directed towards the radar sensor. The received signal is amplified and modulated using an IQ-mixer. The IQ-mixer multiplies the radar signal with a modulation signal comprising of low frequency complex valued sinusoids up to several MHz. The modulation signal for all target elements is provided by a multi-channel digital-to-analog converter (DAC) and thus all modulation signals have a fixed phase relation among each other. The amplitude A_n and phase $\varphi_{\mathrm{mod},n}$ of the modulation signal for the n-th TE can be set arbitrarily. The frequency f_{mod} of the modulation signal for
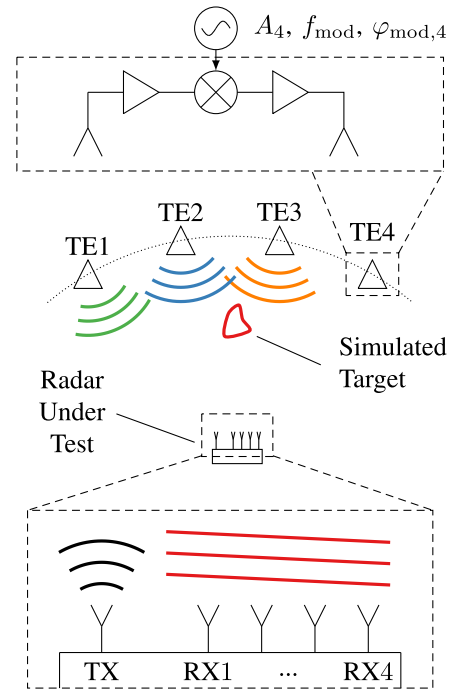

FIGURE 1. System setup view with one transmit and four receive antennas of the radar ($M = 4$). Combined the TEs simulate a target with an arbitrary DoA property. The system design for each TE is displayed at the example of TE4.

all TEs is identical and determines the range and velocity information for a simulated target. By choosing an appropriate modulation frequency f_{mod}, both range and velocity of a target can be simulated. A detailed description of target simulation for CS-FMCW radars by modulating the radar signal can be found in [7], [16], [17]. Following the modulation, the signal is amplified again in order to compensate for the conversion losses, and lastly transmitted by an antenna back towards the radar.

For a radar with a single transmit (TX) antenna and M receive (RX) antennas, the received signal of the m-th antenna will be the superposition of the transmitted signals of all TEs. By tuning the freely selectable amplitudes A_n and phases $\varphi_{\mathrm{mod},n}$ of the TEs, a target with an arbitrary DoA can be simulated, as shown later. In order to adjust the radar cross section (RCS) of a target, the amplitudes A_n can be scaled, causing an increase or decrease of the received signal power at the radar. The simulation of multiple targets with individual DoAs is possible by superimposing the modulation signals of the individual targets in the digital domain before the DAC.

In order to calculate the required amplitudes A_n and phases $\varphi_{\mathrm{mod},n}$ of the TEs, a calibration is performed estimating the channel between the radar under test and the target simulator. Additionally with the information provided by the calibration, placement errors are compensated for CS-FMCW radars. The compensation relaxes the required placement accuracy of the TEs and the radar sensor.

The system concept is also applicable for target elements that generate the range of simulated targets using a delay
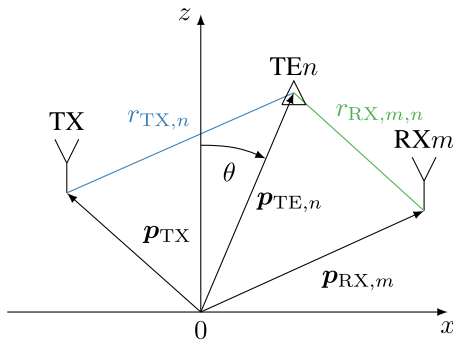
FIGURE 2. Coordinate system and position vectors of the antennas of the radar and the *n*-th TE for an arbitrary placement.

method but modulate the Doppler frequency onto the transmit signal. Therefore, the presented concept is not limited to purely modulation based target simulators. If differences for the concept occur due to the delay method architecture, they will be mentioned explicitly in the following.

III. SIGNAL MODEL

To derive the amplitudes A_n and phases φ_n of the TEs, a suitable coordinate system is introduced. Then, the relation of the received signal at the radar under test is derived with respect to the placement, amplitudes, and phases of the TEs. Subsequently, the influence and compensation of path length differences is analyzed. Eventually, the ideal placement of the TEs and the radar is derived. The signal model will assume a uniform linear array (ULA) of the radar antennas. In the following, variables for vectors are denoted as lower case bold letters and variables for matrices as upper case bold letters.

A. COORDINATE SYSTEM

The coordinate system for an arbitrary placement of the radar and the *n*-th TE is shown in Fig. 2. The antennas of the radar and the TEs are assumed to be at the same height ($y = $ const.) and the Cartesian coordinate system is reduced to two dimensions without loss of generality. The positions of the antennas and TEs are described by their position vector $\boldsymbol{p}$

$$\boldsymbol{p} = \begin{bmatrix} x \\ z \end{bmatrix} = \begin{bmatrix} R \sin(\theta) \\ R \cos(\theta) \end{bmatrix}. \tag{1}$$

All positions relate to the origin of the global coordinate system. The distance between the TX antenna and the *n*-th TE is denoted as $r_{\text{TX},n}$. The distance between the *n*-th TE and the *m*-th RX antenna is denoted as $r_{\text{RX},m,n}$. Consequently, the distance $r_{m,n}$ that a wave travels when it is transmitted by the TX antenna, modulated by the *n*-th TE and retransmitted back to the *m*-th RX antenna of the radar is given by

$$\begin{aligned} r_{m,n} &= r_{\text{TX},n} + r_{\text{RX},m,n} \\ &= |\boldsymbol{p}_{\text{TE},n} - \boldsymbol{p}_{\text{TX}}| + |\boldsymbol{p}_{\text{RX},m,n} - \boldsymbol{p}_{\text{TE},n}|. \end{aligned} \tag{2}$$

B. RECEIVE SIGNAL

The signal transmitted by the radar is modulated by the TEs and transmitted back towards the RX antennas. The superposition of the radar transmit signal, modulated by all N TEs, is therefore received at the *m*-th RX antenna. The received signal $s_{\text{RX},m}(t)$ at the *m*-th RX antenna can be described by

$$s_{\text{RX},m}(t) = \sum_{n=1}^{N} L_{m,n} s_{\text{TX}}(t - T_{m,n}) s_{\text{mod},n}(t) \tag{3}$$

with the modulation signal of the *n*-th TE

$$s_{\text{mod},n}(t) = A_n e^{j(2\pi f_{\text{mod}} t + \varphi_{\text{mod},n})}. \tag{4}$$

The factor $L_{m,n}$ is the loss of the transmission path, and $s_{\text{TX}}(t - T_{m,n})$ is the transmit signal of the radar delayed by the propagation time

$$T_{m,n} = \frac{r_{m,n}}{c_0}. \tag{5}$$

Additive white gaussian noise (AWGN) is neglected in the signal model due to the direct line of sight between the radar and the TEs, resulting in a high signal-to-noise ratio. First, it is assumed that the path length $r_{m,n}$ and the resulting time delay $T_{m,n}$ only cause a constant phase shift $\phi_{m,n}$ for the radar signal with the center frequency f_0 and resulting free-space wavelength λ_0 of

$$\phi_{m,n} = \frac{2\pi}{\lambda_0} r_{m,n} = 2\pi f_0 T_{m,n}. \tag{6}$$

The resulting beat frequency of each TE is similar, since all TEs are placed at the same distance to the radar, and the modulation frequency f_{mod} is identical, justifying this assumption for the time being. The analysis of the error caused by approximating the FMCW signal as a CW signal is considered in Section III-D. With this assumption the receive signals in (3) can be expressed via a matrix vector multiplication

$$\boldsymbol{s}_{\text{RX}}(t) = \boldsymbol{C} \cdot \boldsymbol{s}_{\text{mod}}(t) s_{\text{TX}}(t) \tag{7}$$

with the receive signal vector

$$\boldsymbol{s}_{\text{RX}}(t) = \begin{bmatrix} s_{\text{RX},1}(t) \\ \vdots \\ s_{\text{RX},M}(t) \end{bmatrix}, \tag{8}$$

the modulation vector

$$\boldsymbol{s}_{\text{mod}}(t) = \begin{bmatrix} A_1 e^{j(2\pi f_{\text{mod}} t + \varphi_{\text{mod},1})} \\ \vdots \\ A_N e^{j(2\pi f_{\text{mod}} t + \varphi_{\text{mod},N})} \end{bmatrix} \tag{9}$$

and the complex valued channel matrix

$$\boldsymbol{C} = \begin{bmatrix} L_{1,1} e^{j\phi_{1,1}} & \cdots & L_{1,N} e^{j\phi_{1,N}} \\ \vdots & \ddots & \vdots \\ L_{M,1} e^{j\phi_{M,1}} & \cdots & L_{M,N} e^{j\phi_{M,N}} \end{bmatrix}. \tag{10}$$
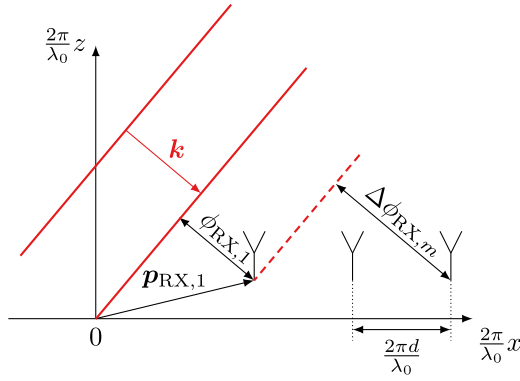
FIGURE 3. Incidenting wave front originating from a target in the far field at the angle θ_{sim}.

The channel matrix $\boldsymbol{C} \in \mathbb{C}^{M \times N}$ contains the entire phase and amplitude relation between the TX antenna and the RX antennas via the TEs. If the number of TEs and RX antennas is identical ($M = N$), the channel matrix $\boldsymbol{C}$ is quadratic. As a result, the freely selectable parameters A_n and $\varphi_{\text{mod},n}$ of the target elements can be determined for a given receive vector using the inverse of $\boldsymbol{C}$. The modulation frequency f_{mod} is the same for all target elements for a given simulated target with a certain range and velocity. Since the focus of this article is the DoA, the modulation frequency f_{mod} will be dropped in the further analysis. For the calculation of f_{mod} see [6], [7]. In order to derive the generation of a DoA for targets by tuning the amplitude A_n and the modulation phase $\varphi_{\text{mod},n}$, the general influence of a DoA is of interest [18]. To simulate a target with a DoA, the phases at the receive antennas must be adjusted to the values that an incidenting wave reflected by a target in the far field of the radar causes. Since the estimation of the DoA is performed at the radar by evaluating the phase difference between the antennas [18], the phase difference between the receive antennas has to be simulated accordingly by the radar target simulator. The reflection of a target in the far field at the angle θ_{sim} will create a plane wave with wavelength λ_0, described by the wave vector

$$\boldsymbol{k} = \frac{2\pi}{\lambda_0} \begin{bmatrix} -\sin(\theta_{\text{sim}}) \\ -\cos(\theta_{\text{sim}}) \end{bmatrix}. \tag{11}$$

The projection of the position of a receive antenna onto the plane wave yields the received phase

$$\phi_{\text{RX},m} = \boldsymbol{k}^\top \cdot \boldsymbol{p}_{\text{RX},m} + \phi_0. \tag{12}$$

The phase offset ϕ_0 describes the phase of the wave at the origin of the coordinate system. As can be seen in Fig. 3, in the special case of a ULA, the phase difference between the first and m-th receive antenna in the array with spacing d parallel to the x-axis at a free-space wavelength λ_0 can be expressed as

$$\begin{aligned} \Delta\phi_{\text{RX},m}(\theta) &= \phi_{\text{RX},m}(\theta) - \phi_{\text{RX},1}(\theta) \\ &= -\frac{2\pi}{\lambda_0} d (m-1) \sin(\theta). \end{aligned} \tag{13}$$

To simulate a target at the DoA θ_{sim} with the target simulator setup, the required steering vector containing all the phases $\Delta\phi_{\text{RX},m}$ is multiplied with the inverse of the channel matrix $\boldsymbol{C}$ to determine the amplitude A_n and phase $\varphi_{\text{mod},n}$ parameters of each target element. A target with a unity amplitude and DoA θ_{sim} can be simulated by the modulation signal phasor vector $\underline{s}_{\text{mod}}$ of

$$\begin{aligned} \underline{s}_{\text{mod}}(\theta_{\text{sim}}) &= \begin{bmatrix} A_1 e^{j\varphi_{\text{mod},1}} \\ \vdots \\ A_N e^{j\varphi_{\text{mod},N}} \end{bmatrix} \\ &= \left(\boldsymbol{C} \cdot \boldsymbol{C}_{\text{comp}} \right)^{-1} \begin{bmatrix} e^{j\Delta\phi_{\text{RX},1}(\theta_{\text{sim}})} \\ \vdots \\ e^{j\Delta\phi_{\text{RX},N}(\theta_{\text{sim}})} \end{bmatrix}. \end{aligned} \tag{14}$$

The compensation matrix $\boldsymbol{C}_{\text{comp}}$ is applied to compensate for path length differences and is derived in subsection III-D. If no compensation is applied, this matrix is the identity matrix $\boldsymbol{I}_N$. By multiplying the resulting signal phasor vector $\underline{s}_{\text{mod}}$ with a scalar so that all modulation amplitudes A_n scale identically, the RCS of the target can be adjusted. Since the channel matrix $\boldsymbol{C}$ has to be invertible, its properties are analyzed in the following.

C. THE CHANNEL MATRIX

In order to analyze the channel matrix $\boldsymbol{C}$ and its invertibility ($M = N$), the channel matrix is calculated for a scenario with the TEs positioned in the far field. Without loss of generality, the path loss is neglected in the following, i.e., $L_{m,n} = 1$. The phase of the channel matrix is split into two matrices:

$$\boldsymbol{C} = \boldsymbol{C}_{\text{RX}} \cdot \boldsymbol{C}_{\text{TX}}. \tag{15}$$

The matrix $\boldsymbol{C}_{\text{TX}}$ accounts for the phase originating from the path between the TX antenna and the target elements $r_{\text{TX},n}$. The phase shift caused by the paths between the TX antenna and the TEs is for each receive antenna path identical. This results in N phases

$$\phi_{\text{TX},n} = \frac{2\pi}{\lambda_0} r_{\text{TX},n}. \tag{16}$$

Therefore,

$$\boldsymbol{C}_{\text{TX}} = \begin{bmatrix} e^{j\phi_{\text{TX},1}} & & 0 \\ & \ddots & \\ 0 & & e^{j\phi_{\text{TX},N}} \end{bmatrix}. \tag{17}$$

The phase relation between a TE and each receive antenna differs in the far field by the phase progression related to the angle θ_{TE}. Consequently, the resulting receive channel matrix is

$$\boldsymbol{C}_{\text{RX}} = \begin{bmatrix} c_{\text{RX},1,1} & \cdots & c_{\text{RX},1,N} \\ \vdots & \ddots & \vdots \\ c_{\text{RX},N,1} & \cdots & c_{\text{RX},N,N} \end{bmatrix} \tag{18}$$

with the elements

$$c_{\text{RX},m,n} = \exp\left[j \left(\phi_{\text{RX},1,n} + \Delta\phi_{\text{RX},m}\left(\theta_{\text{TE},n}\right) \right) \right]. \quad (19)$$

This matrix is closely related to a Vandermonde matrix. When factoring out the constant phase term $\phi_{\text{RX},1,n}$ in (19), which describes the phase shift that results from the path length between the n-th TE and the first RX antenna $r_{\text{RX},1,n}$, from $\boldsymbol{C}_{\text{RX}}$, a Vandermonde $\boldsymbol{C}_{\text{RX},V}$ matrix remains:

$$\boldsymbol{C}_{\text{RX}} = \boldsymbol{C}_{\text{RX},V} \cdot \hat{\boldsymbol{C}}_{\text{RX}} \quad (20)$$

with

$$\hat{\boldsymbol{C}}_{\text{RX}} = \begin{bmatrix} e^{j\phi_{\text{RX},1.1}} & & 0 \\ & \ddots & \\ 0 & & e^{j\phi_{\text{RX},1,N}} \end{bmatrix} \quad (21)$$

and the Vandermonde matrix

$$\boldsymbol{C}_{\text{RX},V} = \begin{bmatrix} 1 & 1 & \cdots & 1 \\ v_1 & v_2 & \cdots & v_N \\ v_1^2 & v_2^2 & \cdots & v_N^2 \\ \vdots & \vdots & \ddots & \vdots \\ v_1^{(N-1)} & v_2^{(N-1)} & \cdots & v_N^{(N-1)} \end{bmatrix} \quad (22)$$

with

$$v_n = e^{j\Delta\phi_{\text{RX},2}(\theta_{\text{TE},n})}. \quad (23)$$

The phase difference between the first and second RX antenna $\Delta\phi_{\text{RX},2}(\theta_{\text{TE},n})$ is calculated by (13). A Vandermonde matrix has a non-zero determinant if the values v_n are distinct [19]. This is the case if every $\theta_{\text{TE},n}$ is distinct and in the unambiguous region of the antenna array. Ambiguity can cause identical v_n entries, even though the corresponding placement angles $\theta_{\text{TE},n}$ are different. This occurs for ULAs if the antenna spacing of the RX array fulfills $d > \lambda_0/2$. Therefore only angles should be chosen, which cause the phase difference to be $|\Delta\phi_{\text{RX},2}(\theta_{\text{TE},n})| < \pi$, the unambiguous region. The matrices $\boldsymbol{C}_{\text{TX}}$ and $\hat{\boldsymbol{C}}_{\text{RX}}$ are also always invertible since they are diagonal matrices with full rank. Therefore, the channel matrix $\boldsymbol{C}$ is invertible as long as two TEs are not placed at the same azimuth angle $\theta_{\text{TE},n}$ towards the radar. In practice, not only identical but also similar angles of the TEs have to be avoided, since similar placement angles $\theta_{\text{TE},n}$ cause the Vandermonde matrix $\boldsymbol{C}_{\text{RX},V}$ to become ill-conditioned. Therefore, in subSection III-E the angular placement of the TEs is presented to achieve a well-conditioned channel matrix.

D. ANALYSIS AND COMPENSATION OF PATH LENGTH DIFFERENCES

The assumption made in (6) that the path length $r_{m,n}$ only creates a constant phase shift $\phi_{m,n}$ is only correct for continous wave (CW) signals. The frequency modulation of a CS-FMCW radar will cause different beat frequencies for each TE if the path lengths $r_{m,n}$ are different. The inversion of the channel matrix and the subsequent vector-matrix multiplication presume phasors of the same frequency. This assumption
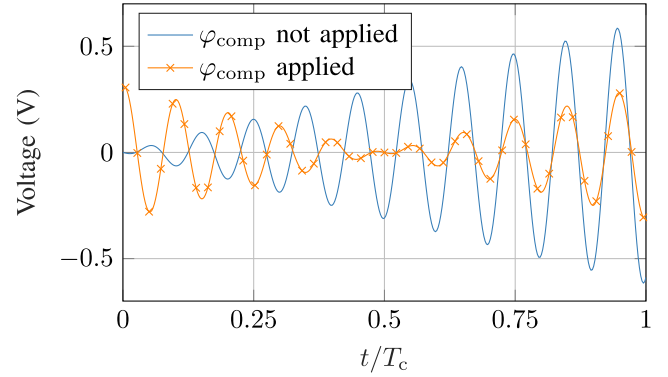
FIGURE 4. Superposition of two sinusoids with a frequency difference $\Delta f < 1/T_c$ and a starting phase difference of π (φ_{comp} not applied) and $\pi - \pi\Delta fT_c$ (φ_{comp} applied).

is therefore not correct, and the impact of the frequency shift is analyzed.

The frequency difference Δf caused by a path length difference of Δr for a CS-FMCW radar with bandwidth B and chirp duration T_c is

$$\Delta f = \Delta r \frac{B}{T_c c_0}. \quad (24)$$

The data aquisition, performed by the radar and consequently the sampling of each ramp, only occurs during the chirp duration T_c, and the frequency difference Δf will cause a continously increasing phase difference of the beat frequency starting from zero up to

$$\Delta\phi_{t=T_c} = 2\pi \Delta r \frac{B}{c_0} = 2\pi \Delta fT_c \quad (25)$$

at the end of a ramp. The effect of this phase drift is best visible when adding two signals with a small frequency difference $\Delta f < 1/T_c$ that have a phase difference of π at $t = 0\,\text{s}$ and the same amplitude. Considering phasors with no frequency difference, the superposition of these signals results in a signal of zero. But due to the frequency difference, the superposition will cause a beat signal with increasing amplitude in the time domain. Compensating the frequency difference by using different modulation frequencies is not possible, since this would violate the constant phase relation between the TEs. Instead, to reduce the error, which means reducing the energy of the superposition signal as close to zero as possible, the phase difference is instead chosen as

$$\Delta\varphi = \pi - \pi\Delta fT_c = \pi + \varphi_{\text{comp}}. \quad (26)$$

The compensation phase φ_{comp} enables calculations as close as possible to phasors with identical frequencies and approximates the CW case. As can be seen in Fig. 4, the compensation phase φ_{comp} shifts the minimum of the superposition into the center of the time interval and thus minimizes its energy. If the radar target simulator employs a delay-based method for creating the range information, the differing range can also be compensated by adjusting the time delay.
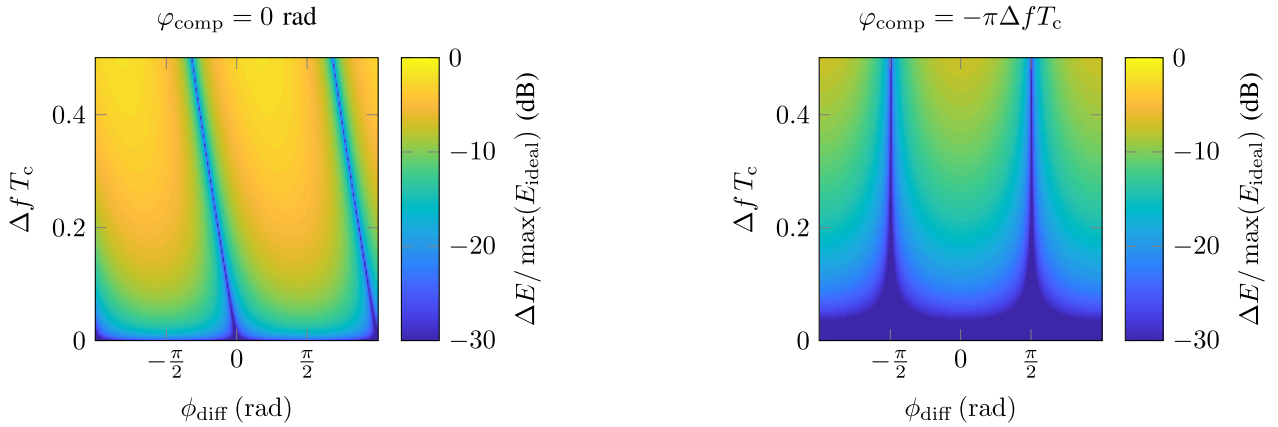
$\varphi_{\mathrm{comp}} = 0 \, \mathrm{rad}$ $\varphi_{\mathrm{comp}} = -\pi\Delta f T_{\mathrm{c}}$

FIGURE 5. Resulting energy error from the addition of two sinusoids with a frequency difference of Δf and a phase difference of ϕ_{diff} in (27) compared to the resulting energy from sinusoids with the same frequency. The left plot shows the resulting energy error without the application of the compensation phase φ_{comp}. The right plot shows the resulting energy error if of the compensation phase φ_{comp} is applied.

In Fig. 5 the energy of the superposition of two TEs with a path length difference of Δr and a resulting frequency difference of Δf of the form

$$E(\Delta f, \phi_{\mathrm{diff}}) = \int_0^{T_{\mathrm{c}}} \left| e^{\mathrm{j}2\pi f t} + e^{\mathrm{j}(2\pi(f+\Delta f)t+\phi_{\mathrm{diff}}+\varphi_{\mathrm{comp}})} \right|^2 \mathrm{d}t \tag{27}$$

is compared with the energy that results from phasors with the same frequency

$$E_{\mathrm{ideal}}(\phi_{\mathrm{diff}}) = \int_0^{T_{\mathrm{c}}} \left| e^{\mathrm{j}2\pi f t} + e^{\mathrm{j}(2\pi f t+\phi_{\mathrm{diff}})} \right|^2 \mathrm{d}t . \tag{28}$$

The resulting energy error $\Delta E = |E - E_{\mathrm{ideal}}|$ is depicted in Fig. 5 with and without the application of the compensation phase φ_{comp}. The resulting energy error can be reduced significantly by applying the compensation phase φ_{comp}. This means that with the application of φ_{comp} the approximation of the superposition of the TEs by phasors causes a smaller error.

For calculating the compensation phase terms, the path length differences are determined during the calibration process. Due to the amount of path the lengths $r_{m,n}$, there will be MN compensation phase terms $\varphi_{\mathrm{comp},m,n}$. However, the compensation phase caused by unaccurate placement of the TEs (differing distance from the center point), will be similar for each receive antenna. A single compensation phase per TE has to be used to preserve the difference between the received phases that are described by $C_{\mathrm{RX,V}}$ in (22). Hence, the arithmetic mean of the compensation phases for each TE

$$\varphi_{\mathrm{comp},n} = \frac{1}{M} \sum_m^M \varphi_{\mathrm{comp},m,n} \tag{29}$$

forms the channel compensation matrix

$$C_{\mathrm{comp}} = \begin{bmatrix} e^{\mathrm{j}\varphi_{\mathrm{comp},1}} & & 0 \\ & \ddots & \\ 0 & & e^{\mathrm{j}\varphi_{\mathrm{comp},N}} \end{bmatrix} . \tag{30}$$
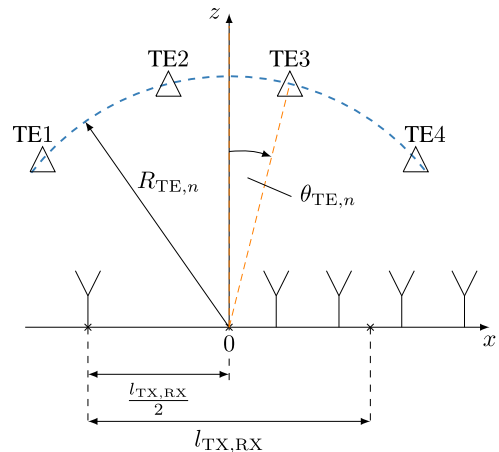

FIGURE 6. Example for an optimal placement of the TEs with an angle of $\theta_{\mathsf{TE},n}$ around the center point located equidistant between the transmit antenna and the center of the receive antenna array. The optimum angles for the TEs in this case (four receive antennas with a spacing of $d = \lambda_0/2$ and four TEs) is $-48°$, $-14°$, $14°$, and $48°$. The radar's location minimizes occuring path length differences by placing the midpoint between the radar's TX antenna and RX antenna array at the origin of the coordinate system.

The compensation phase $\varphi_{\mathrm{comp},n}$ introduces an absolute phase offset, but since only the phase difference between RX antennas is of importance for the DoA estimation, it does not introduce an additional error.

E. OPTIMAL PLACEMENT

Since path length differences impact the performance of the system, the optimum position of the radar is determined which reduces the occuring path length differences. Besides, the optimum placement of the TEs should yield the most robust DoA simulation regardless of placement errors. The optimal placement for a radar sensor with four RX antennas is shown in Fig. 6. The distance of the TEs with respect to the origin of the coordinate system is identical, hence

$$R_{\mathrm{TE},1} = R_{\mathrm{TE},n} \quad n = 1 \ldots N . \tag{31}$$

To achieve the most robust angular placement of the TEs $\theta_{\text{TE},n}$, the possible steering vectors of the radar must be covered uniformaly by the TE positions. Due to the $\sin(\theta)$ component of the phase difference in (13), the DoA resolution at DoAs close to $\theta = \pm 90°$ is lower than at DoAs close to $\theta = 0°$. Consequently, the TEs are placed accordingly to replicate the angular dependency of the resolution. The angles of the TEs $\theta_{\text{TE},n}$ are chosen in order to create uniformly distributed receive differences $\Delta\phi_{\text{RX},2}(\theta_{\text{TE},n}) \in [-\pi, \pi)$. The TE angle spacing is a function of the radar receive antenna spacing d. The optimum angular spacing for simulating DoAs within the entire unambigous region of the radar is

$$\theta_{\text{TE},n} = \sin^{-1}\left(\left(-1 + \frac{2n-1}{N}\right)\frac{2\sin^{-1}\left(\frac{\lambda}{2d}\right)}{\pi}\right). \quad (32)$$

Choosing this spacing turns the Vandermonde Matrix $C_{\text{RX,V}}$ in (22) into a Discrete Fourier Transform (DFT) related matrix, because v_n are equally spaced complex numbers on the unit circle, and $C_{\text{RX,V}}$ is therefore ideally conditioned [20]. If only a field of view is required to be simulated that is smaller than the placement of the outer TEs, with $\theta_{\max} = \max|\theta_{\text{sim}}| < \theta_{\text{TE},N}$, the alternative spacing of

$$\hat{\theta}_{\text{TE},n} = \sin^{-1}\left(\left(-1 + \frac{2n-2}{N-1}\right)\sin(\theta_{\max})\right) \quad (33)$$

should be used. In practice the radiation pattern of a single element of the radar antenna array will determine $\theta_{\max}$, since it limits the effective field of view. Using the spacing of (33) reduces high losses due to target elements being placed outside the effective field of view of the radar. The spacing is constructed by placing the outer target elements (TE1 and TEN) at $\pm\theta_{\max}$. The other elements are then placed to create uniformly distributed receive differences $\Delta\phi_{\text{RX},2}(\hat{\theta}_{\text{TE},n})$ within this region.

Since the placement of the RX- and TX antennas influences the resulting path lengths of the individual TEs, the position of the radar is chosen to minimize the longest occuring path length difference

$$\Delta l_{\max} = \max_{m,n,h} |r_{m,n} - r_{m,h}| \quad m, n, h = 1, 2, \ldots N. \quad (34)$$

As discussed in subSection III-D, path length differences alter the superposition of the retransmitted TE signals for a single target. In Fig. 7 a simulation of the maximum resulting path length difference $\Delta l_{\max}$ for different positions of the radar is depicted. The simulation result is achieved under the assumption that the TX antenna and RX antennas have a fixed spacing $l_{\text{TX,RX}}$, set by the radar's manufacturer. Thus, the position of the radar is determined by the position of the TX antenna. The minimum path length difference occurs at an x-offset of $l_{\text{TX,RX}}/2$ and a z-offset of zero and therefore, the center should be chosen halfway between the position of the TX antenna and the center of the RX antenna array. In Fig. 7 it can be also seen that the placement in x-direction is more crucial than in z-direction.
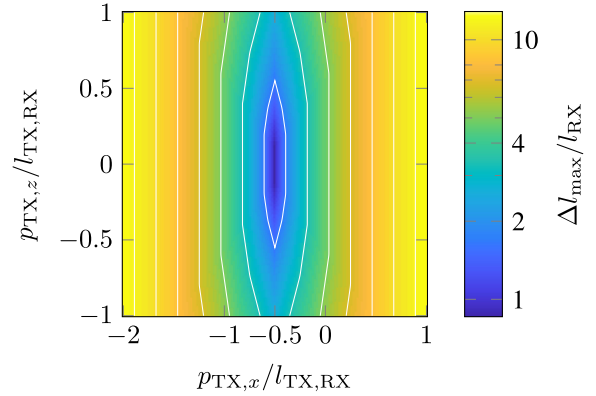

FIGURE 7. Maximum occuring path length difference $\Delta l_{\max}$ for different placements of the radar, determined by the position of the TX antenna p_{TX}. The length of the RX antenna array is $l_{\text{RX}} = (N-1)d$.

IV. CALIBRATION PROCESS

In order to estimate the losses $L_{m,n}$, phase shifts $\phi_{m,n}$, and path length differences $\Delta r_{m,n}$, a calibration must be perfomed. The calibration estimates the channel matrix C and the path length differences for the calculation of the compensation matrix C_{comp}. To determine the path loss $L_{m,n}$ and phase $\phi_{m,n}$, the magnitude and phase of targets simulated by the TEs in the range-Doppler (Rv) domain are evaluated. All estimated parameters require accurate phase, frequency, and magnitude information. Using a maximum likelihood approach a low frequency mismatch is achieved by maximizing the magnitude level of the target peaks.

The calibration is performed stepwise by using two TEs simultaneously with different modulation frequencies. The path length differences are determined relative to TE1. Therefore, TE1 is always active, and the second active TE is changed between the steps, beginning with TE2 and ending at TEN. If the calibration process is started at an arbitrary point in time t_0 and a single target is generated by TE1 with the modulation frequency f_{mod}, the resulting phase at the m-th receive antenna is described by

$$\phi_{\text{cal},m,1}(t_0) = \phi_{m,1} + 2\pi f_{\text{mod}}t_0 + \varphi_{\text{mod},1}. \quad (35)$$

Thus, the direct estimation of the phase $\phi_{m,1}$ is not possible due to the additional phase term $2\pi f_{\text{mod}}t_0$ caused by the arbitrary point in time. To enable the estimation of the phase terms, a second TE (n-th element) is used at the same time with the modulation frequencies $2f_{\text{mod}}$ and $3f_{\text{mod}}$. The two TEs combined will simulate three targets with three corresponding peaks in the range-Doppler evaluation of the radar. The beat frequencies of the simulated targets at the radar are denoted as f_{p1}, f_{p2}, and f_{p3}. All other TEs are turned off during this calibration step. In Fig. 8 an idealized Rv-plot is shown with the three target peaks, generated by two active TEs. The phases of the target peaks created by the n-th TE can be described as

$$\phi_{\text{cal},m,n}^{\text{I}}(t_0) = \phi_{m,n} + 4\pi f_{\text{mod}}t_0 + \varphi_{\text{mod},n} \quad (36)$$
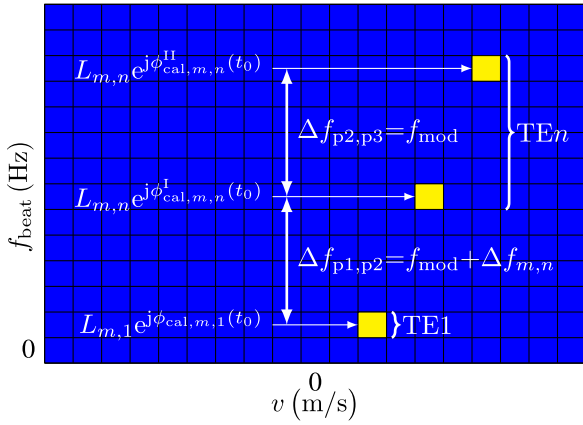
FIGURE 8. Idealized Rv-plot resulting from the calibration step of the n-th TE for the m-th receive antenna. Three targets are generated, one by the first TE and two by the n-th TE. The phase and frequency values need to be extracted for all receive antennas individually.

$$\phi_{\mathrm{cal},m,n}^{\mathrm{II}}(t_0) = \phi_{m,n} + 6\pi f_{\mathrm{mod}}t_0 + \varphi_{\mathrm{mod},n}. \quad (37)$$

By forming the difference of $\phi_{\mathrm{cal},m,n}^{\mathrm{I}}$ and $\phi_{\mathrm{cal},m,n}^{\mathrm{II}}$, the part of the phase which is caused by the random time instance t_0 is calculated:

$$2\pi f_{\mathrm{mod}}t_0 = \phi_{\mathrm{cal},m,n}^{\mathrm{II}}(t_0) - \phi_{\mathrm{cal},m,n}^{\mathrm{I}}(t_0) \quad (38)$$

Therefore, the phase information of the channel matrix C for the two TEs if $\varphi_{\mathrm{mod},1} = \varphi_{\mathrm{mod},n} = 0$ can be calculated via

$$\phi_{m,1} = \phi_{\mathrm{cal},m,1}(t_0) + \phi_{\mathrm{cal},m,n}^{\mathrm{I}}(t_0) - \phi_{\mathrm{cal},m,n}^{\mathrm{II}}(t_0) \quad (39)$$

$$\phi_{m,n} = 3\phi_{\mathrm{cal},m,n}^{\mathrm{I}}(t_0) - 2\phi_{\mathrm{cal},m,n}^{\mathrm{II}}(t_0). \quad (40)$$

The second quantity that needs to be determined is the occuring path-length differences for each receive antenna to calculate the compensation phase via (26). The path-length difference can be estimated from the Rv-plot as well. The two target points created by the n-th TE with the frequencies f_{p2} and f_{p3} will have a range difference corresponding exactly to f_{mod}. The frequency difference between the first and the second target peak $\Delta f_{\mathrm{p1},\mathrm{p2}}$ is however

$$\Delta f_{\mathrm{p1},\mathrm{p2}} = f_{\mathrm{p2}} - f_{\mathrm{p1}} = f_{\mathrm{mod}} + \Delta f_{m,n}, \quad (41)$$

with $\Delta f_{m,n}$ being the frequency shift, caused by the path-length difference

$$\Delta r_{m,n} = r_{m,n} - r_{m,1}. \quad (42)$$

between the two TEs. With the range frequency difference $\Delta f_{m,n}$, the compensation phase $\varphi_{\mathrm{comp},m,n}$ can be calculated by (26). The third parameter, the loss $L_{m,n}$, is determined by the magnitude of the created target peaks by the TEs.

V. SIMULATION RESULTS

To investigate the properties of the system, a simulation is conducted performing the same steps that need to be executed for a deployment of the simulator in practice. First, the TEs are placed, then the calibration is performed, and afterwards, a target with a DoA θ_{sim} is simulated via the TEs. The position
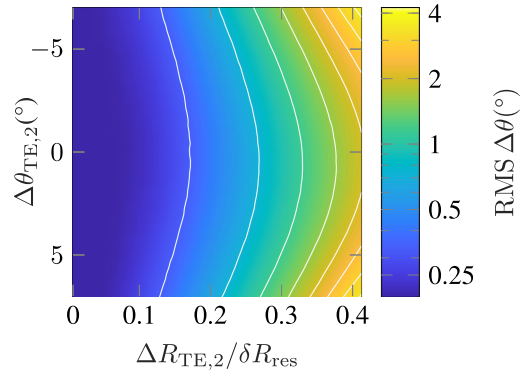

FIGURE 9. Resulting RMS DoA error $\Delta\theta$ of a simulated target for misplacements in angular ($\Delta\theta_{\mathrm{TE,2}}$) and range ($\Delta R_{\mathrm{TE,2}}$) direction of TE2.

of the simulated target is estimated via standard radar signal processing, comprising of constant false alarm rate (CFAR), peak search, and a Bartlett beamformer for the estimated DoA θ_{est}. The simulation is performed with a radar employing one TX and four RX antennas in a ULA configuration. The radar employs a chirp bandwidth B that results in a range resolution of $\delta R_{\mathrm{res}} = c_0/(2B)$. The optimal positions of the TEs and the radar for the simulation are shown in Fig. 7.

Firstly, the influence of placement errors in range direction $R_{\mathrm{TE},n}$ is investigated. If the TEs are placed with different distances $R_{\mathrm{TE},n}$ towards the center point, path length differences are present, which create errors due to the resulting frequency shift. Secondly, the influence of placement errors with respect to the TE angle $\theta_{\mathrm{TE},n}$ is analyzed. Targets with a DoA θ_{sim} between $-70°$ and $70°$ are simulated, and the root mean square (RMS) of the error $\Delta\theta = \theta_{\mathrm{sim}} - \theta_{\mathrm{est}}$ between the intended and estimated DoA is calculated.

In Fig. 9 the RMS of the resulting error $\Delta\theta$ is shown for placement errors in range direction $\Delta R_{\mathrm{TE,2}}$ and angular direction $\Delta\theta_{\mathrm{TE,2}}$ of TE2. If TE2 is placed incorrectly with respect to the angle $\theta_{\mathrm{TE,2}}$, the channel matrix is conditioned worse, but since the resulting phases at the RX antennas are determined during the calibration, they are accounted for during matrix inversion. With increasing errors in distance $\Delta R_{\mathrm{TE,2}}$ the RMS error of the DoA of a simulated target increases significantly, due to the increasing uncompensated path length differences.

To analyze the improvement achieved by compensating path length differences with the compensation phase $\varphi_{\mathrm{comp},n}$, the same simulation is perfomed with C_{comp} applied. The comparison between the compensated and uncompensated target simulation is plotted in Fig. 10. The RMS error includes all simulated DoAs θ_{sim} and angular placement errors $\Delta\theta_{\mathrm{TE,2}}$.

Errors caused by different placement distances are less critical if C_{comp} is applied and hence, the RMS error is lower compared to the uncompensated simulation. If TE2 is placed at different angles than the optimal one, the compensation phase does not lead to any accuracy improvement or degradation. This can be seen in Fig. 9, since with low distance errors $\Delta R_{\mathrm{TE,2}}$ the performance with and without the application of the compensation matrix C_{comp} is identical.
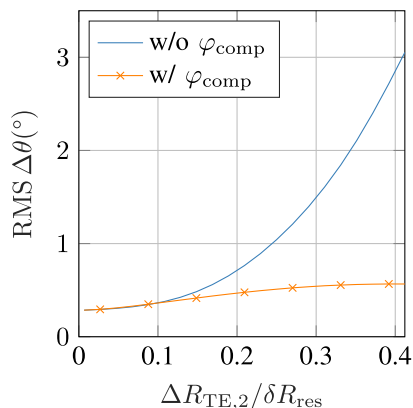
FIGURE 10. Resulting RMS DoA error $\Delta\theta$ of a simulated target for misplacements range ($\Delta R_{\text{TE,2}}$) direction of TE2. The resulting RMS DoA error $\Delta\theta$ with the application of φ_{comp}.
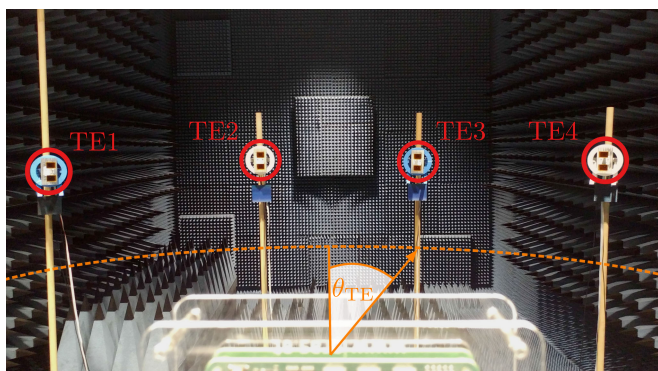

FIGURE 11. Photograph of the measurement setup. The radar is at the bottom of the photo. The TEs are positioned around the radar at the angles θ_{TE} −33°, −10.5°, 10.5°, and 33°.

VI. MEASUREMENTS

The measurement setup consists out of four TEs. Each TE can realize a maximum gain of 13 dB at the highest modulation amplitude A_n between the antenna connections. A side band suppression of 30 dB is achieved by the IQ-mixer, used for the modulation. A CS-FMCW radar was used to verify the approach for the simulation of arbitrary DoAs θ_{sim}. The antenna array of the radar used for the verification has a 6 dB beamwidth of 66° for the combined radiation patterns of the TX- and RX-antennas. A limited simulated field of view of 66° was therefore chosen. The ideal positions for the TEs are according to (33) −33°, −10.5°, 10.5°, and 33°. The measurement setup is shown in Fig. 11 and its parameters are listed in Table I.

In Fig. 12 the magnitude of the Bartlett beamformer DoA estimation, implemented by a 1024-point DFT, is shown. The DoA estimation is performed for the target peak in the range-Doppler plot with the highest magnitude. The DoA estimation result for three simulated DoA values that are between the azimuth positions of the TEs θ_{TE} is shown exemplarily in Fig. 12.

TABLE 1. Overview of Measurement Setup

|	
Ramp duration T_{c}	200 µs
Bandwidth B	1.8 GHz
Range resolution δR_{res}	83 mm
Start frequency	77.2 GHz
Number of RX channels	4
RX antenna spacing d	1.95 mm = $0.5\lambda_0$
Radar RX-TX 6-dB beamwidth	66°
Simulated field of view	66°
TE positions θ_{TE}	±33°, ±10.5°
TE maximum gain	13 dB
TE sideband suppression	30 dB
Distance to target simulator $R_{\text{TE},n}$	2.1 m
Simulated distance of target	6.3 m
Simulated speed of target	3 m s^{-1}
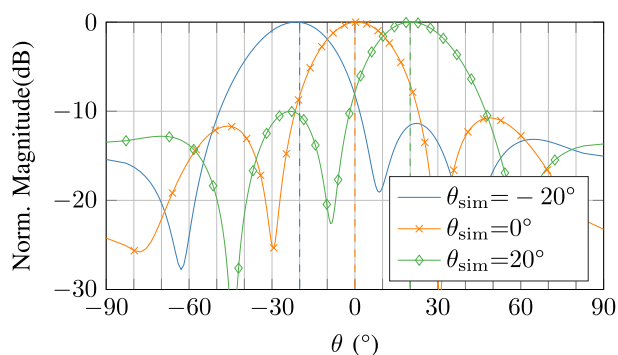
FIGURE 12. \boldmath Magnitude of Bartlett beamformer DoA estimation for simulated DoAs between the angles of TEs. The intended simulated DoAs θ_{sim} are shown as dashed lines.
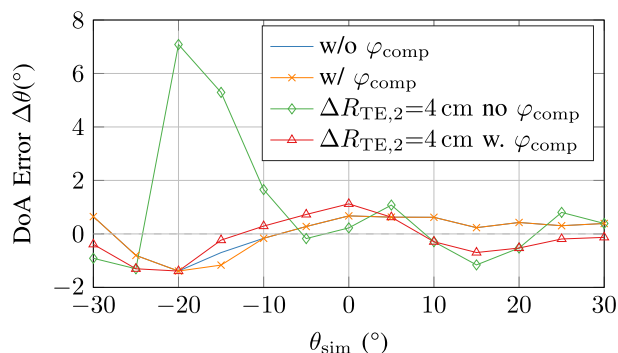

FIGURE 13. Resulting error $\Delta\theta$ between measured DoA and simulated DoA θ_{sim}.

Simulated targets with a DoA θ_{sim} property in 5°-steps were created consecutively to validate the achievable accuracy. In order to confirm the impact of the compensation phase φ_{comp}, a second measurement was perfomed where TE2 was moved 4 cm towards the radar to create an additional path length difference due to inaccurate placement ($\Delta R_{\text{TE,2}}/\delta R_{\text{res}} = 0.5$). In Fig. 13 the error between the intended simulated DoA θ_{sim} and the estimated DoA θ_{est} via a Bartlett beamformer is depicted. For accurately placed TEs, the compensation phase has no significant impact and the deviation from the intended DoA is less than 1.5°. If TE2 is placed with a 4 cm offset
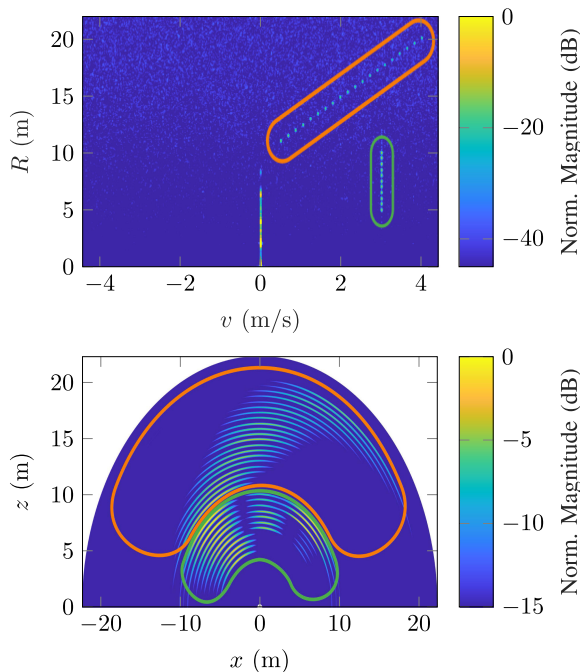
FIGURE 14. Rv-plot of a scenario with 41 simulated targets. The estimated position in the Cartesian coodinate system of moving targets is depicted below. Up to three targets are simulated in a single Rv-cell.

error $\Delta R_{\text{TE},2}$, the accuracy of the generated DoA without the compensation phase will suffer greatly with a deviation up to $7°$ between intended and estimated DoA, while the compensation phase can increase the accuracy to a level close to the accurately placed setup. In order to emphasize the tremendous advantages of the here presented setup for simulating complex scenarios, 41 point scatteres were simulated. In Fig. 14, the resulting Rv-plot and the Cartesian xz-plot are depicted. The estimation of the DoA is performed on targets with a velocity $v \neq 0 \, \text{m s}^{-1}$. The corresponding targets between the Rv-plot and the Cartesian xz-plot are marked by the orange and green borders. For Rv-cells encircled by the green border up to three targets per Rv-cell were simulated. The number of targets per Rv-cell increases with greater distances. This shows that the approach allows the simulation of multiple targets with identical range and velocity but different DoAs. The targets, marked by the orange border, display the continously changeable DoA capability of the setup between $-33°$ and $33°$. The signal used to simulate the scenario is the superposition of the modulation signals for the 41 individual targets, calculated in the digital domain. For each simulated target the required amplitudes and phases of the TEs for the intended DoA is calculated using (14).

VII. CONCLUSION
In this article, a DoA generation approach is presented suitable for target simulators with a modulation capability. With distributed, coherently modulated target elements, a variable DoA generation is achieved solely by tuning the amplitude and phase of the modulation signals employed in the target

elements. The ideal positioning and the compensation of placement errors are discussed and verified with simulations and measurements. A calibration is presented in order to estimate the phase and amplitude relation between the radar and the target elements. With low hardware costs and a high accuracy, arbitrary DoAs for an indefinite amount of targets can be simulated, while maintaining a high reliability due to electrical steering. Besides, several targets can be simulated within a single Rv-cell with differing DoAs. The DoA generation approach exhibits a measured accuracy better than $\pm 1.5°$ for a radar sensor with four receive antennas.

REFERENCES
[1] C. Waldschmidt, J. Hasch, and W. Menzel, "Automotive radar - From first efforts to future systems," *IEEE J. Microwaves*, vol. 1, no. 1, pp. 135–148, Jan. 2021.

[2] F. Roos, J. Bechter, C. Knill, B. Schweizer, and C. Waldschmidt, "Radar sensors for autonomous driving: Modulation schemes and interference mitigation," *IEEE Microw. Mag.*, vol. 20, no. 9, pp. 58–72, Sep. 2019.

[3] J. Dickmann *et al.*, "Automotive radar the key technology for autonomous driving: From detection and ranging to environmental understanding," in *Proc. IEEE Radar Conf.*, 2016, pp. 1–6.

[4] N. Kalra and S. M. Paddock, "Driving to safety: How many miles of driving would it take to demonstrate autonomous vehicle reliability?," *Transp. Res. A, policy Pract.*, vol. 94, pp. 182–193, 2016.

[5] A. Gruber *et al.*, "Highly scalable radar target simulator for autonomous driving test beds," in *Proc. Eur. Radar Conf.*, 2017, pp. 147–150.

[6] J. Iberle, P. Rippl, and T. Walter, "A near-range radar target simulator for automotive radar generating targets of vulnerable road users," *IEEE Microw. Wireless Compon. Lett.*, vol. 30, no. 12, pp. 1213–1216, Dec. 2020.

[7] F. Rafieinia and K. Haghighi, "ASGARD1: A novel frequency-based automotive radar target simulator," in *Proc. IEEE MTT-S Int. Conf. Microw. Intell. Mobility*, 2020, pp. 1–4.

[8] M. Engelhardt, F. Pfeiffer, and E. Biebl, "A high bandwidth radar target simulator for automotive radar sensors," in *Proc. Eur. Radar Conf.*, 2016, pp. 245–248.

[9] J. Schlichenmaier, N. Selvaraj, M. Stolz, and C. Waldschmidt, "Template matching for radar-based orientation and position estimation in automotive scenarios," in *Proc. IEEE MTT-S Int. Conf. Microw. Intell. Mobility*, 2017, pp. 95–98.

[10] K. Werber *et al.*, "Automotive radar gridmap representations," in *Proc. IEEE MTT-S Int. Conf. Microw. Intell. Mobility*, 2015, pp. 1–4.

[11] S. Buddappagari *et al.*, "Over-the-air vehicle-in-the-loop test system for installed-performance evaluation of automotive radar systems in a virtual environment," in *Proc. 17th Eur. Radar Conf.*, 2021, pp. 278–281.

[12] M. E. Asghar *et al.*, "Radar target simulator and antenna positioner for real-time over-the-air stimulation of automotive radar systems," in *Proc. 17th Eur. Radar Conf.*, 2021, pp. 95–98.

[13] W. Scheiblhofer, R. Feger, A. Haderer, and A. Stelzer, "Concept and realization of a low-cost multi-target simgulator for CW and FMCW radar system calibration and testing," *Int. J. Microw. Wireless Technol.*, vol. 10, no. 2, pp. 207–215, 2018.

[14] M. E. Russell and C. A. Drubin, "Automotive forward looking sensor test station," U.S. Patent 6,114,985, Sept. 5, 2000.

[15] V. H. Maples and G. A. Eastman, "Radar scene simulator," U.S. Patent 4,660,0 41, Apr. 21, 1987.

[16] J. Iberle, M. A. Mutschler, P. A. Scharf, and T. Walter, "A radar target simulator concept for close-range targets with micro-doppler signatures," in *Proc. 12th German Microw. Conf.*, 2019, pp. 198–201.

[17] W. Scheiblhofer, R. Feger, A. Haderer, and A. Stelzer, "A low-cost multi-target simulator for FMCW radar system calibration and testing," in *Proc. Eur. Radar Conf.*, 2017, pp. 343–346.

[18] C. Vasanelli *et al.*, "Calibration and direction-of-arrival estimation of millimeter-wave radars: A practical introduction," *IEEE Antennas Propag. Mag.*, vol. 62, no. 6, pp. 34–45, Dec. 2020.

[19] L. M. Milne-Thomson, *The Calculus of Finite Differences*. New York, NY, USA: Macmillan, 1933.

[20] V. Y. Pan, "How bad are vandermonde matrices?," *SIAM J. Matrix Anal. Appl.*, vol. 37, no. 2, pp. 676–694, 2016.

PIRMIN SCHOEDER (Graduate Student Member, IEEE) received the B.Sc. and M.Sc. degrees in 2017 and 2019, respectively, in electrical engineering from the University of Ulm, Ulm, Germany, where he is currently working toward the Ph.D. degree with the Institute of Microwave Engineering.

In 2019, he was an Intern with Rohde & Schwarz, Singapore. His current research interests include system concepts and signal processing for radar target simulators.

VINZENZ JANOUDI received the M.Sc. degree in electrical engineering from the University of Applied Sciences of Karlsruhe, Karlsruhe, Germany, and the M.Eng degree from Ryerson University, Toronto, ON, Canada, in 2018 and 2019, respectively. He is currently working toward the Ph.D. degree in electrical engineering with the Institute of Microwave Engineering, University Ulm, Ulm, Germany.

In 2015 and 2016, he was with Rohde & Schwarz, Munich, as a Bachelor Thesis Student and Development Engineer for software defined radio waveforms. In 2018, he was with Bosch Corporate Research as a Master thesis Student in the field of distributed source coding. From 2019 to 2020, he was with PLATH Group as a Development Engineer for signal intelligence receivers and direction finders. Since 2020, he has been a Research Assistant with the University Ulm. His research interests include communication systems, stochastic signal processing, system concepts for radar networks in the automotive sector, and the accompanying signal processing.

BENEDIKT MEINECKE (Graduate Student Member, IEEE) received the M.Sc. degree in 2017 in electrical engineering with a focus on communication technology from the University of Ulm, Ulm, Germany, where he is currently working toward the Ph.D. degree in electrical engineering with the Institute of Microwave Engineering.

His research interests include system concepts for multistatic coherent radar networks and the accompanying signal processing.

DAVID WERBUNAT (Graduate Student Member, IEEE) received the B.Sc. and M.Sc. degrees in 2017 and 2019, respectively, in electrical engineering from the University of Ulm, Ulm, Germany, where he is currently working toward the Ph.D. degree with the Institute of Microwave Engineering.

His current research interests include digital radar systems and system concepts and signal processing for coherent radar networks.

CHRISTIAN WALDSCHMIDT (Senior Member, IEEE) received the Dipl.-Ing. (M.S.E.E.) and the Dr.-Ing. (Ph.D.E.E.) degrees from the University Karlsruhe, Karlsruhe, Germany, in 2001 and 2004, respectively. From 2001 to 2004, he was a Research Assistant with the Institut für Höchstfrequenztechnik and Elektronik, Universität Karlsruhe. Since 2004, he has been with Robert Bosch GmbH, in the business units Corporate Research and Chassis Systems. He was heading different research and development teams in microwave engineering, rf-sensing, and automotive radar. In 2013, he returned to academia. He was appointed as the Director of the Institute of Microwave Engineering, University Ulm, Ulm, Germany, as Full Professor. He has authored or coauthored more than 200 scientific publications and more than 20 patents. His research topics include on radar and rf-sensing, mm-wave and submillimeter-wave engineering, antennas and antenna arrays, and rf and array signal processing. He is a Member of the Executive Committee Board of the German MTT/AP joint chapter, and Member of the German Information Technology Society. He is Chair of the IEEE MTT-29 Technical Committee on Microwave Aerospace Systems and was the Chair of MTT-27 Technical Committee on Wireless Enabled Automotive and Vehicular Applications. He was a two-time TPC Chair and General Chair of the IEEE MTT International Conference on Microwaves for Intelligent Mobility. Since 2018, he has been an Associate Editor for IEEE MTT MICROWAVE WIRELESS COMPONENTS LETTERS. He is a reviewer for multiple IEEE transactions and many IEEE conferences in the field of microwaves. He was co-recipient of 11 best paper awards since 2014.